# Fabrication of Realistic Transparent Porous Media for 3D Observation of Internal Mass Transport


Taiki Gyotoku[†], Tatsuki Iwaguchi[‡], Shigeto Hanya[†], Shusaku Harada[†*], Yohsuke Tanaka[‡] and Yasufumi Yamamoto[§]

[†] Division of Sustainable Resources Engineering, Faculty of Engineering, Hokkaido University, N13-W8, Sapporo, Hokkaido, 060-8628, Japan

[‡] Faculty of Mechanical Engineering, Kyoto Institute of Technology, Matsugasaki, Sakyo-ku, Kyoto 606-8585, Japan

[§] Department of Mechanical Engineering, Kansai University, 3-35, Yamate-cho 3-chome, Suita, Osaka, 564-8680, Japan

* Corresponding author: Shusaku Harada

Phone/Fax: + (81)-11-7066310

E-mail address: harada@eng.hokudai.ac.jp

## ABSTRACT

A new experimental system was developed to observe the migration of colloidal particles in saturated porous media in 3D, which is important in engineering processes such as contaminant migration and filtration. The system enables the observation of internal migration that are invisible from the outside by fabricating a porous body using a transparent material and a 3D printer. Non-artificial media with arbitrarily controlled internal pore sizes were fabricated by designing the porous media based on the results of numerical analysis on phase separation phenomena. The refractive indices of the porous media and the interstitial liquid were matched, and a laser sheet was used to extract cross-sections of the media. By reconstructing multiple cross-sectional images, it was possible to visualize the 3D migration of suspended particles. The developed system was then applied to the collective gravitational settling of fine particles in saturated porous media. The results showed that the particles selectively settled in the pore networks while repeatedly branching in the lateral direction.

## 1. Introduction

The migration of solutes, particulate materials, and immiscible liquids in saturated porous media is observed in small- to medium-scale engineering devices such as fuel cells and water treatment systems [1,2], and also in large-scale engineering processes such as $CO_2$ geological storage and oil recovery [3-7]. Among these transport phenomena, the migration of colloidal particles in porous media is a fundamental phenomenon in environmental engineering and soil physics, such as contaminant transport and filtration [8-13].

The gravitational settling behavior of fine particles in saturated porous media depends not only on the physical properties and concentration conditions of the particles and fluid, but also on the pore size, pore shape, and its space-filling property in the media. As one of examples, Figure 1 shows the settling behavior of fine particles (wheat flour) in water-saturated gravel layers as reported in our previous study [14]. The gravel diameter is 5 to 10 mm, and the volumetric concentration of the fine particles is 0.2. As seen in the figure, the particles settle collectively and invade specific pores selectively. In this case, the settling velocity is greatly enhanced by the collective motion and is considerably larger than the Stokes settling velocity. As shown in the previous study [14], the gravitational settling behavior of fine particles in saturated porous media shows various settling patterns depending on the pore characteristics as well as the suspended conditions.

However, mass transfer inside saturated porous media, as shown in Fig. 1, cannot be observed from the outside. Therefore, the 3D motions of materials inside porous media are difficult to understand via experiments. Recent studies have developed non-contact measurement techniques for mass transfer in porous media using various techniques, such as fluorescent particle imaging [15, 16], magnetic resonance imaging [17], and X-ray computed tomography [18]. However, most of these techniques observe mass transfer in porous media from an average point of view, and there are few techniques to measure the details of transport phenomena at pore-scales. The present study aims to construct an experimental system that can quantitatively evaluate 3D mass transfer in porous media, especially the migration of colloidal particles in individual pores. This allows us to know the details of transport phenomena related to the above-mentioned engineering problems.

This study accomplishes three objectives: The first objective is to design a realistic porous geometry that eliminates artificial factors. The second is to fabricate a porous body using transparent

Fig.1 Collective settling of wheat flour–water suspension in saturated gravel layer at volumetric concentration $\phi = 0.2$. The images were captured 10 seconds apart [14].

materials. The final objective is to develop a system for observing mass transfer in arbitrary cross sections inside porous media. This article is organized as follows. In Chapter 2, the design of porous materials through numerical analysis of phase decomposition is described. In Chapter 3, the fabrication of transparent porous materials is explained. In Chapter 4, the 3D observation method of mass transfer inside porous media, which uses reflective index (RI) matching and laser scanning techniques, is introduced. Finally, the proposed method is adopted to observe mass transfer in porous media, i.e., collective settling of particles in saturated media, as a demonstration.

## 2. Design of Realistic Porous Materials

Porous materials have various types, such as particle-filled layers and fracture networks. In this study, the design requirements of porous media are: 1) no isolated voids, 2) parametrically adjustable pore sizes, and 3) lack of artificial factors. In this study, we attempted to design a porous body based on spinodal decomposition. As is well-known, spinodal decomposition is known as a phase decomposition without nucleation, which results from thermodynamic fluctuation. It occurs in the separation of mixtures of metals and in some mineral formations. Recently, spinodal decomposition has been used to generate architected materials [19] and to set boundary conditions in the numerical analyses of certain phenomena in complicated porous materials [20]. The dynamics of spinodal

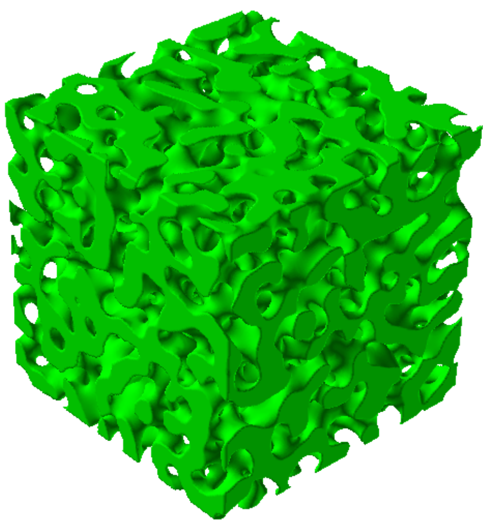

Fig.2 Example of porous material design based on spinodal decomposition.

decomposition is generally modeled using the following equation as a suitable rescaling of the Cahn–Hilliard equation [20, 21].

$$\frac{\partial \psi}{\partial t} = \frac{1}{2} \nabla^2 (-\psi + \psi^3 - \nabla^2 \psi), \tag{1}$$

where $\psi$ is the order parameter. In this study, the solid region is represented by a negative $\psi$, the void region by a positive $\psi$ and the interface by $\psi = 0$. Equation (1) contains both diffusion and inverse diffusion terms and consequently a network-like phase separation proceeds from the mixing of the two phases.

Figure 2 shows an example of a structure obtained via spinodal decomposition. Such a structure

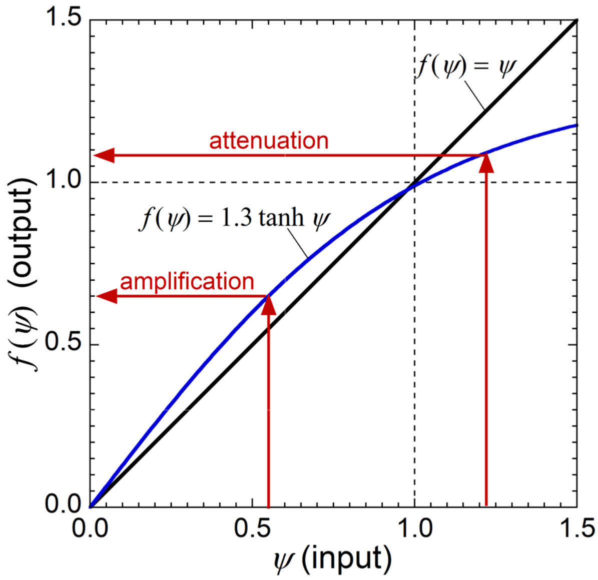


Fig.3 Map function mimicking inverse diffusion effect.

satisfies the above-mentioned requirements: a connected pore structure, control of pore size, and elimination of artificial factors. To solve Eq. (1) numerically, we employ the computationally efficient method proposed by Oono and Puri [22] and also used by Chakrabarti [20]. This method adopts a map function $f$ to mimic the inverse diffusion effect originating from the free energy functional as follows:

$$f(\psi) = 1.3 \tanh \psi. \tag{2}$$

As shown in Figure 3, for positive values of $\psi$, this map function returns an amplified value for $\psi < 1$ and an attenuated value for $\psi > 1$, so the returned value approaches one with the same sign of $\psi$ and same behavior for negative values. Through this mapping, the order parameter values in most parts of the solid region approach $-1$ and those in the void region approach $1$, thus the interface is sharpened. The diffusion term in Eq. (1) is represented by a Laplacian operator using a spatial average $\langle \ \rangle$ as follows via a 3D-extended form of the 2D procedure of Oono and Puri [22],

$$\begin{aligned} \langle\psi\rangle = \frac{1}{24}\Big[2\sum(\psi \text{ in the nearest-neighbor cells}) \\ + \sum(\psi \text{ in the next-nearest-neighbor cells})\Big]. \end{aligned} \tag{3}$$

Using these elements, we solve Eq. (1) in an equally-arranged 3D cell space $(i, j, k)$ in time steps of $(n)$, similar to Oono and Puri [22]. (i) Tentative new step values $\psi^{*}_{i,j,k}$ are calculated by the following inverse diffusion and diffusion terms,

$$\psi^{*}_{i,j,k} = f\left(\psi^{(n)}_{i,j,k}\right) + D\left(\langle\psi^{(n)}_{i,j,k}\rangle - \psi^{(n)}_{i,j,k}\right), \tag{4}$$

where $D$ is the diffusion coefficient. (ii) For the conservation of the order parameter inside the neighborhood surrounding the current cell, the new step values are updated by the changed portion of the order parameter as follows:

$$\psi^{(n+1)}_{i,j,k} = \psi^{*}_{i,j,k} - \langle\psi^{*}_{i,j,k} - \psi^{(n)}_{i,j,k}\rangle, \tag{5}$$

Figure 4 shows an example of the numerical results of spinodal decomposition obtained by the method described above. The number of cell points is $256^3$, and periodic boundary conditions are set in three directions. The initial condition was given by a random number between $-0.1$ and $0.1$ as the order parameter for each cell. We set the diffusion coefficient $D = 0.5$ and 1,000,000 steps of time advancement were performed. We confirmed the total value of the order parameters to be almost zero in any step, so the void fraction $\varepsilon$ is kept being 0.5. Figure 4 shows that a connected pore network develops and the pore size increases as time progresses. From these data, we can select

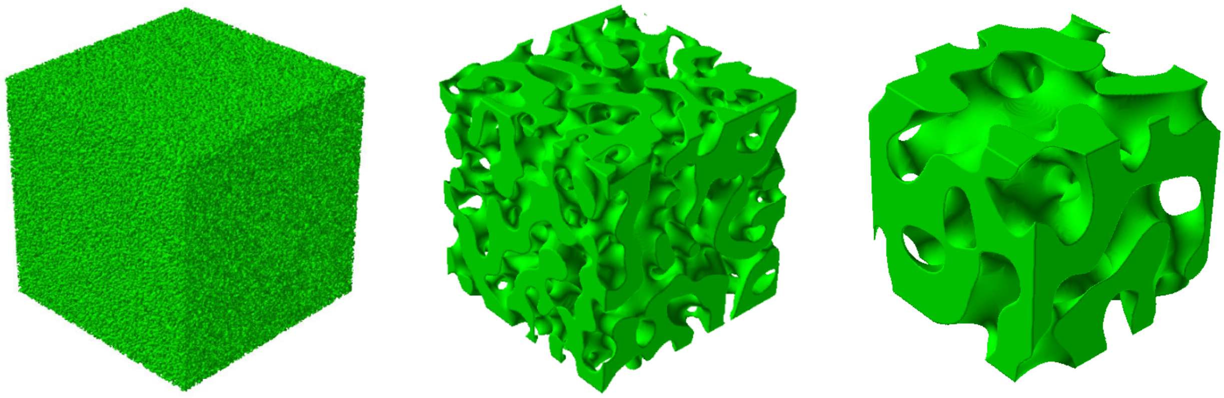

(a) initial condition (b) 100,000th step (c) 1,000,000th step

Fig.4 Numerical results of spinodal decomposition, visualized using isosurfaces of $\boldsymbol{\psi} = \mathbf{0}$. The bounds of the computational domain of the solid region were padded using $\boldsymbol{\psi} = \mathbf{0}$ (the originally simulated data are treated using periodic boundaries) to clarify the solid regions.

instantaneous data that have suitable pore scales, as described later.

## 3. Fabrication of Porous Materials

### 3.1 Design of porous material with arbitrary pore size

Structures with arbitrary pore sizes are extracted from the numerical results of spinodal decomposition, which is explained in the previous section, to generate a blueprint for fabricating porous materials. Therefore, representative pore sizes are quantified for each step of the numerical analysis. For permeate flow in porous media, the average hydraulic diameter $L_p$ is given as follows,

$$L_p = \frac{4V}{A} = \frac{4\varepsilon L^3}{A}, \tag{2}$$

where $V(= \varepsilon L^3)$ is the pore volume, $L$ is the region size, $\varepsilon$ is the void ratio and $A$ is the wetted surface area. If the average hydraulic diameter $L_p$ is considered as the representative pore size, the wetted surface area $A$ is required.

In our simulation code, the triangulation process of isosurfaces is implemented via level contour reconstruction [23], which is used in the front-tracking multiphase flow simulations [24]. Therefore, we compute the wetted area by simply summing the areas of all triangle elements. The nondimensional region length $L = 256$ is scaled to the longest side length of the real model (set according to the 3D printer configuration, as described later), and then the dimensional average

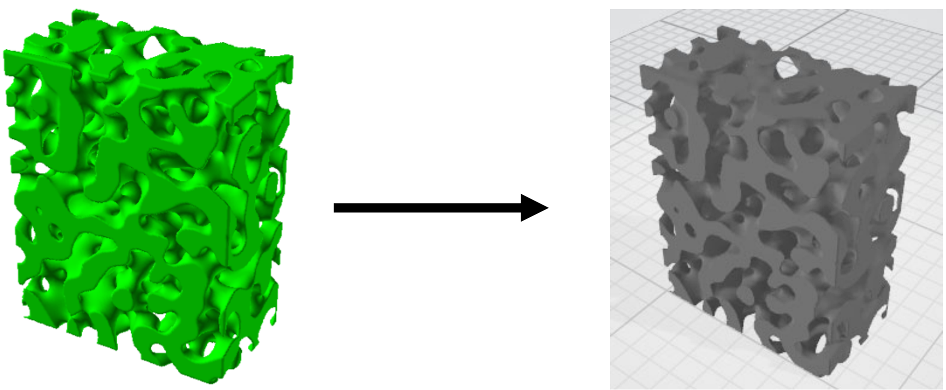

Fig.5 Isosurface graphics of numerical results visualized using AVS/Express and 3D viewer image of the corresponding STL data ($L_p$ = 6.0 mm).

hydraulic diameter $L_p$ is obtained. The output data of the shorter sides in the numerical simulations are trimmed and the outer bounds of the solid region are padded using $\psi = 0$.

Extracted structures at an arbitrary pore scale must be saved in a file format that can be recognized by a 3D printer. In this study, the numerical results (isosurface of $\psi = 0$) described in the previous section are displayed as polygon graphics using the visualization software (AVS/express Developer) and saved as STL format files, as shown in Fig. 5. This process enables the fabrication of actual porous materials using a 3D printer.

## 3.2 Fabrication of transparent porous materials

A transparent porous material was fabricated using an optical fabrication machine. The STL file is

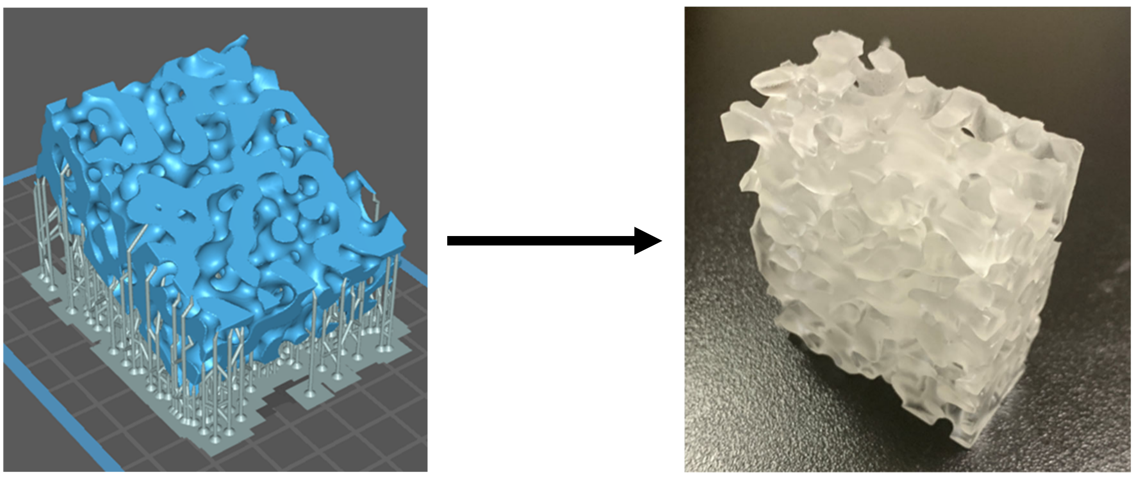

Fig.6 Fabricated transparent porous material ($L_p$ = 6.0 mm).

edited using CG softwares (Blender 2.93, Flashprint 5) for trimming (size control) and supplementing with support materials. Using the edited STL file, porous structures are fabricated using the optical fabrication machine (Elegoo, Mars 3) with high transparency resin (SK Honpo, SK01CR). Figure 6 shows an example of edited STL file and a porous object fabricated using the optical fabrication machine. Fig. 6 shows that the product is almost identical in appearance to the blueprint. A detailed comparison between them is shown below.

Figure 7 shows transparent porous materials fabricated in this study at various pore scales (average hydraulic diameter $L_p$ ). All structures are sized 24 mm × 48.5 mm × 59 mm. As can be seen in the figure, a difference of 1 mm in the average hydraulic diameter $L_p$ results in a significant variation in appearance. To maintain transparency, the surface was not treated with ultraviolet light, as is generally practice. Nevertheless, the produced resin was not completely transparent, as shown in

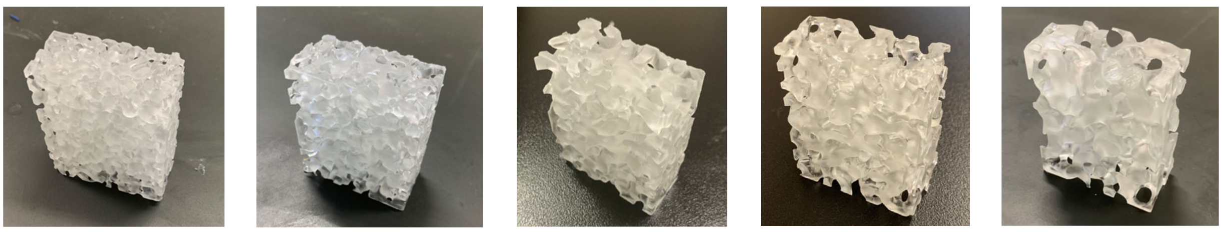

(a) $L_p$ = 4.0 mm (b) $L_p$ = 5.0 mm (c) $L_p$ = 6.0 mm (d) $L_p$ = 7.0 mm (e) $L_p$ = 8.0 mm

Fig.7 Transparent porous materials fabricated at various pore scales.

Fig.7. We attempted to enhance transparency using a surface coating agent, but gave it up due to the difficulty of applying a uniform coating, even to the internal pores.

## 4. Visualization of Internal Structure

### 4.1 RI matching

As mentioned in the Introduction, this study aims to achieve the observation of mass transfer inside saturated porous media. Therefore, we attempted to visualize the internal structure of materials by adjusting RI of the fluid that fills the porous media. In this study, multiple fluids with different RIs

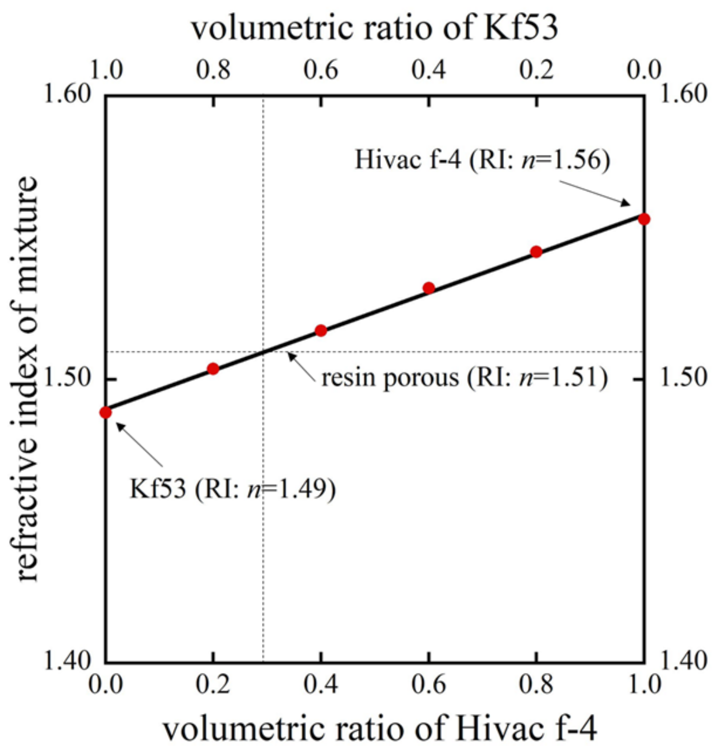


Fig.8 Refractive index of fluid mixtures with various mixing ratios.

were mixed to match the RI of the resin, forming the porous media. The RI of the resin (solid), as measured using a refractometer, is 1.51. Therefore, silicone oil with RI of 1.49 (Shin-Etsu Chemical, Kf53) and that with RI of 1.56 (Shin-Etsu Chemical, Hivac f-4) were mixed at various ratios. Figure 8 shows the measured RI of fluid mixtures with various mixing ratios. The RI of the mixture with a ratio of approximately 1:3 matches that of the resin when mixed. Figure 9 shows images of the produced porous material filled with water (left) and silicone oil mixtures (right). Whereas the porous material is not transparent in water, it is visible to the naked eye in silicone oil and the grid paper behind is not distorted.

(a) in water (b) in silicone oil

Fig.9 Appearance of fabricated porous materials in fluids.

## 4.2 Laser scanning

The inside of the saturated porous material with RI matching was observed by a laser scanning system. The left part of Figure 10 shows an overview of the laser scanning system. A laser sheet source (Japan Laser, DPGL-1W), a camera (FLIR, FL3-U3-13Y3) with a variable focal length lens (Edmund Optics, Varifocal Lens 9-90mm) and a mirror are mounted on a metal frame fixed on a linear translation stage (Oriental Motor, DRSM42RG). The translation stage is controlled by a personal computer with a maximum translation speed of 50 mm/s and a minimum translation distance of 0.001 mm.

A laser sheet irradiates the experimental vessel vertically to extract the internal cross-section of

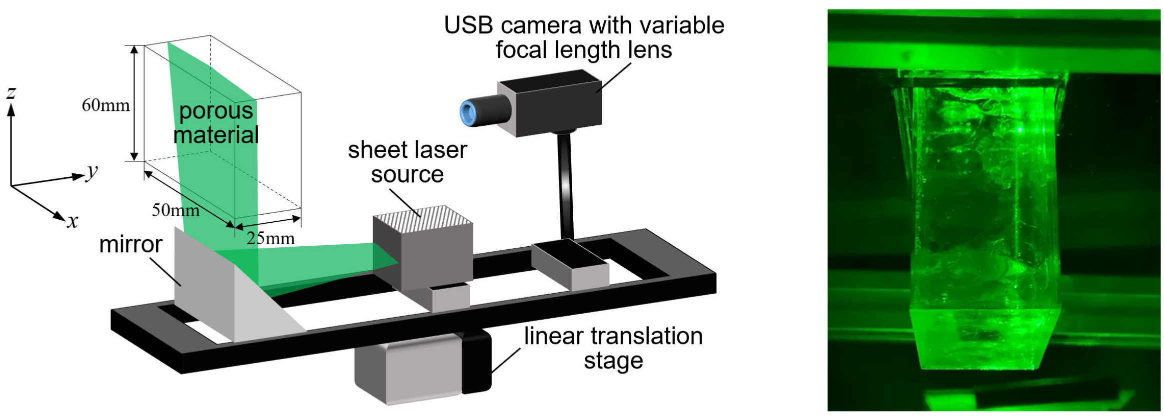


Fig.10 Laser scanning system (left: experimental equipment, right: laser-irradiated porous material).

the porous media, as shown in the right part of Fig.10. The translational stage moves the laser sheet horizontally and stops at arbitrary positions. The camera captures cross-sectional images of the porous media. Then 3D images inside the porous media are obtained by reconstructing the cross-sectional images at each instant of time.

### 4.3 Visualization of internal pore structure

Figure 11 shows cross-sectional views at an arbitrary positions obtained from the original STL file (top images), and the cross-sectional images of the manufactured porous material visualized by laser

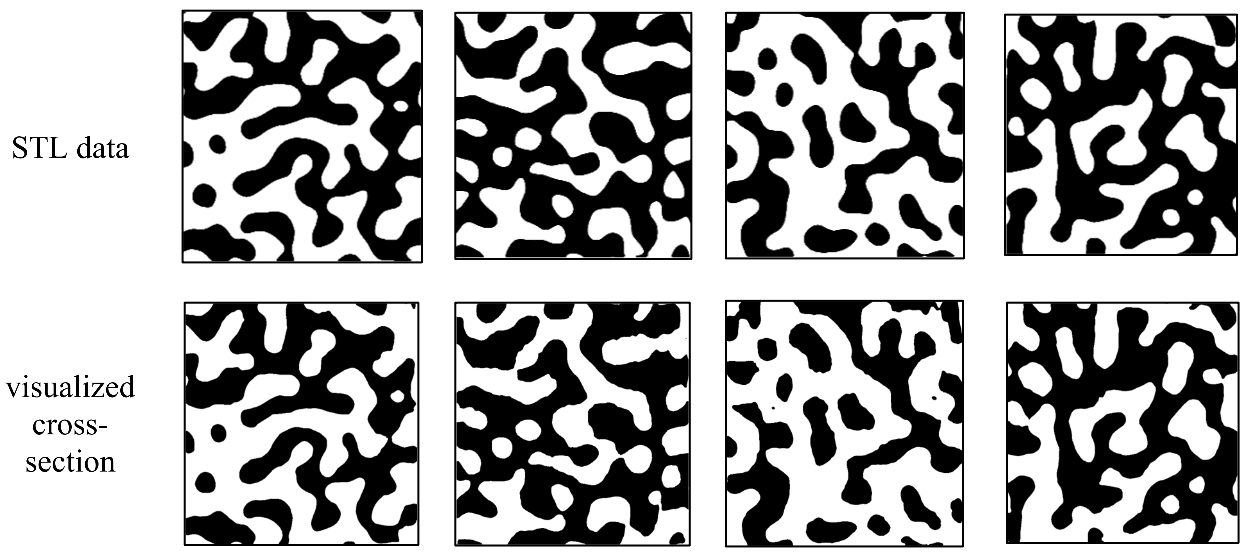


(a) $y$=2.15 mm (b) $y$=7.50 mm (c) $y$=12.60 mm (d) $y$=17.15 mm

Fig.11 Comparison of internal pore structures (top: STL data, bottom: visualized cross-section).

scanning at the same positions (bottom images). As seen in the Fig. 11, the cross-sectional shape of the fabricated porous material matches that obtained from the design (STL file), with the exception of a few minor differences. For a quantitative comparison, the difference between the STL file and visualized data was determined by subtracting the cross-sectional images, and the average areal difference was 7 % at four cross-sections shown in Fig.11. Therefore, we succeeded in fabricating transparent porous materials that allows us to observe its internal structure, which is the objective of this study.

## 4.4 Application to 3D visualization of mass transport in porous material

Finally, mass transfer visualization experiment were conducted using the experimental system developed in this study. The system was applied to the gravitational settling of the particulate suspension in saturated porous media, as shown in Fig. 1. Figures 12 and 13 show the collective settling behavior of solid particles at each cross-sectional position in a porous material with a pore scale of $L_p$ = 6.0 mm. The suspended particles are monodisperse glass particles with a narrow size distribution. The average particle diameter is $d_p$ = 60 μm and the particle concentration is $\phi$ = 0.01.

Figure 14 shows a 3D reconstructed image created from 11 cross-sectional images under the same condition as Figs.12 and 13.

Since the resolution of each image shown in Figs. 12 to 14 is approximately 0.07 mm/pixel, which is larger than the particle diameter, the present system cannot directly detect individual particles. Therefore, the red area shown in each figure represents the existence region of particles rather than individual particles. Figs.12 to 14 represent that suspended particles invade into many pores complicatedly. In individual cross-sectional images (Fig.12), the particles appear to exist in isolated

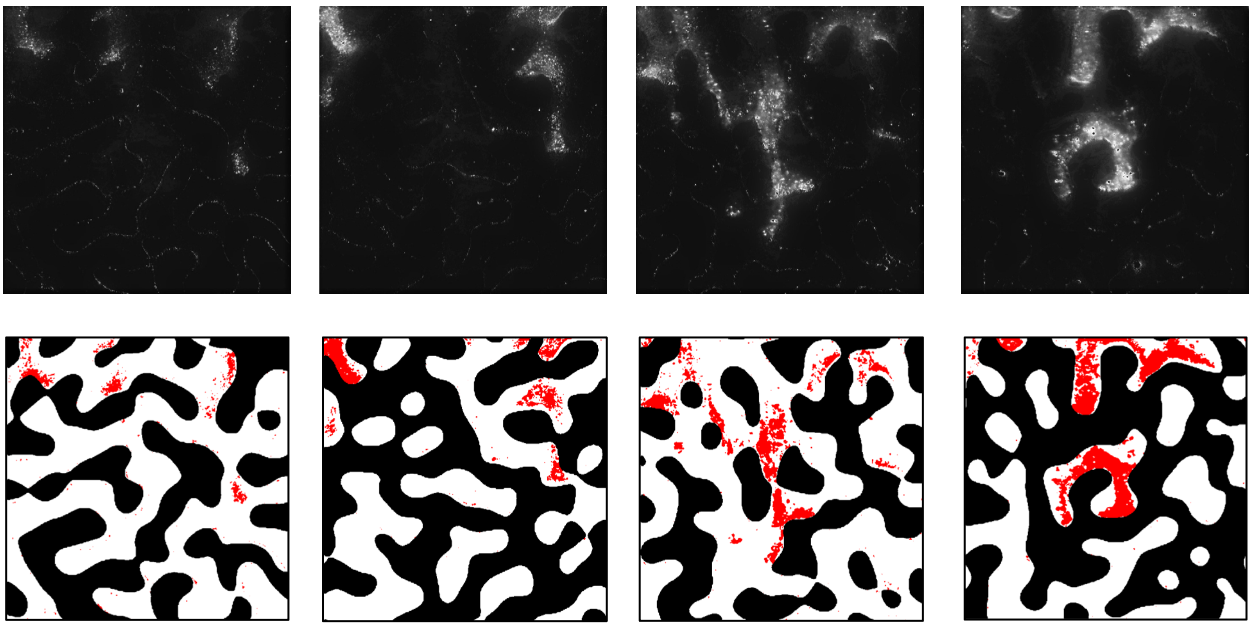

(a) $y = 5$ mm (b) $y = 9$ mm (c) $y = 13$ mm (d) $y = 17$ mm

Fig.12 Cross-sectional visualization of collective settling of particles in saturated porous media (upper: visualized cross-sectional images, lower: existing region of suspended particles).

Fig.13 Sequence of cross-sectional images displayed at intervals of every 2 mm in $y$ direction.

pores. This is because the particles migrate laterally in the connected pore networks as shown in Figs.13 and 14.

The previous study [14] have reported that the gravitational settling behavior of fine particles in saturated porous media are complex and depends not only on the physical properties of the particles and fluid, but also on the pore size. More quantitatively, the settling pattern of particles varies with the dimensionless number $(L_p/d_p)\ \phi^{1/2}$ ($L_p$: representative pore size) from individual to collective settling [14, 25]. In the experimental condition shown in Figs.12 to 14, the corresponding dimensionless number is $(L_p/d_p)\ \phi^{1/2}$=10, which is close to the collective condition [25]. Under the collective condition, the particles settle collectively similar to a continuous fluid, and invade several pores in saturated porous media. Figs.12, 13 and 14 clearly show such collective behaviors of

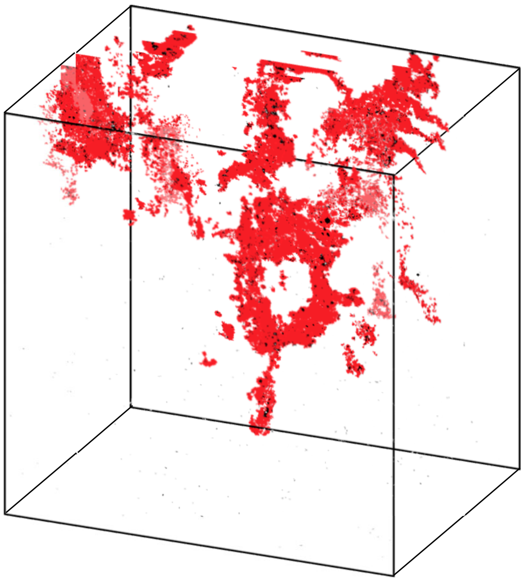

Fig.14 3D constructed image of settling particles in saturated porous media.

suspended particles.

As indicated by these results, the experimental system developed in this study enables the observation of the migration of fine particles inside porous media, which generally cannot be observed from the outside. Using this system, it is possible to capture mass transfer at individual pore-scales. The measurement limits of this system depend on many factors, i.e., the limit of the fabrication of 3D pore structure, the thickness of the sheet laser, and the spatial resolution of the acquired images. With the present system, it is impossible to detect individual particles when using particles of several tens of microns, but it is possible to identify the existing region of particles in individual pores of several millimeters. With the further development of the system, it would be possible to measure mass transfer in porous materials with pore sizes of less than 1 mm.

## 5. Conclusion

A new experimental system was developed to visualize mass transfer inside a saturated porous materials from the outside. Porous media were fabricated using transparent materials, and the refractive indices of the liquid filling the pores were matched with those of the media to enable the observation of the internal structure of the saturated materials. The liquid was a mixture of two types of silicone oil, and the mixing ratio was adjusted to obtain the appropriate RI.

A numerical simulation of phase separation by spinodal decomposition was performed to design a porous material with an arbitrary pore size without artificial factors. The structures observed during the separation of the two phases were extracted, and the boundary surfaces were used in the design of the porous media.

Cross-sectional observation of the inside of the porous media was performed using a laser sheet, and a distortion-free cross-sectional image was obtained. The cross-sectional shape of the fabricated porous media was compared with the results of spinodal decomposition analysis, and the findings showed that the design was accurately reproduced except for some minor differences.

Finally, the collective gravitational settling of fine particles in the porous media was observed using the system developed in this study. The results showed that the system exhibited complex behavior, such as the collective settling of particles in selective pore networks. As mentioned above, the measurement system developed in this study is capable of continuously changing the pore size. Therefore, the system can provide detailed information on mass transfer in porous media at various pore scales.

## Acknowledgement

This study was supported by JSPS KAKENHI Grant No.19H02058 and 23H01334.

## References

[1] Wang, C.-Y., Fundamental Models for Fuel Cell Engineering, *Chem. Rev.*, vol. **104**, pp. 4727–4765, 2004.

[2] Bijeljic, B., Mostaghimi, P. and Blunt, M. J., Signature of Non-Fickian Solute Transport in Complex Heterogeneous Porous Media, *Phys. Rev. Lett.,* vol. **107**, 204502, 2011.

[3] Blunt M. J. and King, M. J., Simulation and Theory of Two-Phase Flow in Porous Medium.

*Phys. Rev. A*, vol. **46**, no.12, pp. 7680–7699, 1992.

[4] Setiawan, A., Nomura H. and Suekane, T., Microtomography of Imbibition Phenomena and Trapping Mechanism, *Transp. Porous Med.,* vol. **92**, pp. 243–257, 2012.

[5] Zhang, C., Kaito, K., Hu, Y., Patmonoaji, A., Matsushita S. and Suekane, T., Influence of Stagnant Zones on Solute Transport in Heterogeneous Porous Media at the Pore Scale, *Phys. Fluids*, vol. **33**, 036605, 2021.

[6] Riaz, A., Hesse, M., Tchelepi, H. A. and Orr, F. M., Onset of Convection in a Gravitationally Unstable Diffusive Boundary Layer in Porous Media, *J. Fluid Mech.*, vol. **548**, pp. 87–111, 2006.

[7] Akai, T., Kuriyama, T., kato, S. and Okabe, H., Numerical Modelling of Long-term $CO_2$ Storage Mechanisms in Saline Aquifers Using the Sleipner Benchmark Dataset, *Int. J. Greenhouse Gas Control*, vol. **110**,103405, 2021.

[8] Sen, T. K., Mahajan S. P. and Khilar, K. C., Colloid-Associated Contaminant Transport in Porous Media: 1. Experimental Studies, *AIChE J.,* vol. **48**, no. 10, pp. 2366–2374, 2002.

[9] Edery, Y., Scher, H. and Berkowitz, B., Particle Tracking Model of Bimolecular Reactive Transport in Porous Media, *Water Resour. Res.*, vol. **46**, W07524, 2010.

[10] Magal, E., Weisbrod, N., Yechieli, Y., Walker S. L. and Yakirevich, A., Colloid Transport in Porous Media: Impact of Hyper-saline Solutions, *Water Res.* vol. **45**, no.11, pp. 3521–3532, 2011.

[11] Wang, Y., Xu L., Chen H. and Zhang, M., Retention and Transport Behavior of Microplastic Particles in Water-Saturated Porous Media, *Sci. Total Environ.,* vol. **808**, 152154, 2022.

[12] Tu, S., Liu X. and Cai, H., Effect of Gravity on Colloidal Particle Transport in a Saturated Porous Medium: Analytical Solutions and Experiments, *PLos ONE*, vol. **17**, no.10, e0275644, 2022.

[13] Chrysikopoulos, C. V. and Syngouna, V. I., Effect of Gravity on Colloid Transport through Water-Saturated Columns Packed with Glass Beads: Modeling and Experiments, *Environ. Sci. Technol.*, vol. **48**, pp. 6805–6813, 2014.

[14] Gyotoku, T., Masuda, M., Nishimura, K., Harada, S., Tanaka Y. and Yamamoto, Y. Variation in the Settling Behavior of Particulate Suspension in Saturated Gravel Layers, *J. Porous*

*Med.,* 10.1615/JPorMedia.2023046565, 2022

[15] Thomas J. M. and Chrysikopoulos, C. V., A New Method for In Situ Concentration Measurements in Packed-Column Transport Experiments, *Chem. Eng. Sci.*, vol. **65**, pp. 4285–4292, 2010.

[16] Chrysikopoulos, C. V., Plega C. C. and Katzourakis, V. E., Non-invasive In Situ Concentration Determination of Fluorescent or Color Tracers and Pollutants in a Glass Pore Network Model, *J. Hazard. Mater.*, vol. **198**, pp.299–306, 2011.

[17] Lakshmanan, S., Holmes, W. M., Sloan W. T. and Phoenix, V. R., Nonoparticle Transport in Saturated Porous Medium Using Magnetic Resonance Imaging, *Chem. Eng. J.*, vol. **266**, pp. 156–162, 2015.

[18] Wang, L., Nakanishi, Y., Teston A. D. and Suekane, T., Effect of Diffusing Layer Thickness on the Density-Driven Natural Convection of Miscible Fluids in Porous Media: Modeling of Mass Transport, *J. Fluid Sci. Tech.*, vol.**13**, jfst0002, 2018.

[19] Shimizu R. and Tanaka, H., Impact of Complex Topology of Porous Media on Phase Separation of Binary Mixtures, *Sci. Adv.*, vol. **3**, eaap9570, 2017.

[20] Chakrabarti, A., Kinetics of Domain Growth and Wetting in a Model Porous Medium, *Phys. Rev. Lett.*, vol. **69**, pp.1548–1551, 1992.

[21] Grant, M., Miguel, M. S., Viñals J. and Gunton, J. D., Theory for the Early Stages of Phase Separation: the Long-Range-Force Limit, *Phys. Rev. B*, vol.**31**, pp.3027–3039, 1985.

[22] Oono Y. and Puri, S., Computationally Efficient Modeling of Ordering of Quenched Phases, *Phys. Rev. Lett.*, vol. **58**, pp.836–839, 1987.

[23] Shin, S. and Juric, D., Modeling Three-Dimensional Multiphase Flow Using a Level Contour Reconstruction Method for Front-Tracking without Connectivity, *J. Comp. Phys.*, vol. **180**, pp. 427–470, 2002.

[24] Yamamoto, Y., Ito, T., Wakimoto T. and Katoh, K., Numerical and Theoretical Analyses of the Dynamics of Doplets Diven by Electrowetting on Dielectric in a Hele-Shaw Cell, *J. Fluid Mech*., vol. **839**, pp. 468–488, 2018.

[25] Yamamoto, Y., Hisataka F. and Harada, S., Numerical Simulation of Concentration Interface in Stratified Suspension: Continuum-Particle Transition, *Int. J. Multiphase Flow*, vol. **73**,

pp.71–79, 2015.